

# Chapter 1

## A Particle Detection Method for MA-TIRFM and Its Application

### 1.1 Introduction

Total internal reflection fluorescence microscopy (TIRFM) is widely used in biological experiments to acquire images of small particles near the cell membrane due to its unique illumination mechanism. A single TIRF image is just a projection of the 3D volume in the evanescent field, and it can not provide 3D information. A new generation of TIRFM, multi-angle TIRFM (MA-TIRFM), can reveal the 3D information of the particles by using 2D images taken at different incident angles. Since it is a relatively new technique, only a few applications have been developed to measure relatively large biological structures [?, ?], e.g., microtubules and secretary granules.

In this chapter, we present a MAP based method for particle feature estimation in 3D using MA-TIRFM. In section 5.2, we describe the simplified image model, and present the MAP framework for feature estimation. In section 5.3, we describe the simulation settings, and report the evaluation results on synthetic datasets. In section 5.4, we show the application to studying the properties of CCP particles' motion. In section 5.5, we conclude this chapter.

## 1.2 Method

### 1.2.1 The Simplified Particle Image Model

The particle image model for multi-angle TIRF microscopy is essentially the same as that for single-angle TIRF microscopy. In TIRF microscopy, when the incident angle  $\theta_n$  of the laser beam exceeds the critical angle, total internal reflection will occur at the interface of two mediums (glass and specimen) with different refractive indices. In the evanescent field generated near the interface, the fluorophores are excited to emit fluorescence light. The axial profile of the evanescent field [?, ?] can be well described by an exponential decay function  $h_n(z) \doteq I_{0n} \exp(-z/d_n)$ .  $d_n$  is the penetration depth, and  $I_{0n}$  is the intensity at the interface. The fluorescence light is captured by an EMCCD camera. The image  $I_n(x, y)$  from the EMCCD camera is determined by the input fluorescence signal  $f_n(x, y)$  and the noise sources. By using a set of incident angles  $\{\theta_n\}_{n=1}^N$  with penetration depths  $\{d_n\}_{n=1}^N$ , a set of 2D images  $\{I_n(x, y)\}_{n=1}^N$  can be obtained. The particle image model at each angle  $\theta_n$  has been introduced in chapter 3, and it is used in simulation. That model is simplified to be used for feature estimation, as described in the following paragraphs.

The fluorescence signal  $f_n(x, y)$  is modeled as the sum of Gaussian mixture  $G_n(x, y)$  and background  $b_n(x, y)$ , given by

$$f_n(x, y) \doteq G_n(x, y) + b_n(x, y) \quad (1.1)$$

The background  $b_n(x, y)$  is spatially smooth. The Gaussian mixture  $G_n(x, y)$  has  $K$  components, i.e.,  $G_n(x, y) = \sum_{k=1}^K G_n^{(k)}(x, y)$ . Each component  $G_n^{(k)}(x, y)$  corresponds to a particle with a feature vector  $[x^{(k)}, y^{(k)}, z^{(k)}, r^{(k)}, c^{(k)}]$ , given by

$$G_n^{(k)}(x, y) = a_n^{(k)} \exp \left[ -\frac{(x - x^{(k)})^2 + (y - y^{(k)})^2}{2(r^{(k)})^2} \right] \quad (1.2)$$

Here,  $(x^{(k)}, y^{(k)}, z^{(k)})$  is the center position of the particle  $k$ , and  $r^{(k)}$  is the radius.  $a_n^{(k)}$  is the amplitude of the fluorescence signal associated with the angle  $\theta_n$ . Using Eq.(3.19) and Eq.(4.4), we

obtain the expression of  $a_n^{(k)}$ , given by

$$a_n^{(k)} = \bar{c}_n^{(k)} h_n(z^{(k)}) \quad (1.3)$$

$$\begin{aligned} \bar{c}_n^{(k)} &= 3c^{(k)}(d_n/\epsilon^{(k)})^3 [(\epsilon^{(k)}/d_n)\cosh(\epsilon^{(k)}/d_n) \\ &\quad - \sinh(\epsilon^{(k)}/d_n)](\sigma_p/r^{(k)})^2 \end{aligned} \quad (1.4)$$

$$c^{(k)} = \frac{4}{3}\pi(\epsilon^{(k)})^3\rho^{(k)} \quad (1.5)$$

Here,  $\rho^{(k)}$  is the fluorescence density of the fluorophores in the particle, and  $\epsilon^{(k)}$  is the real radius of the particle.  $c^{(k)}$  is the total fluorescence intensity of the particle in the 3D space.  $\sigma_p$  is the parameter of the point spread function defined in Eq.(3.10). Usually  $\epsilon^{(k)}$  is smaller than each penetration depth  $d_n$  and the parameter  $\sigma_P$ , then we obtain the approximation of Eq.(5.3), given by

$$a_n^{(k)} \approx c^{(k)}h_n(z^{(k)}) \quad (1.6)$$

The image  $I_n(x, y)$  associated with the angle  $\theta_n$  is determined by the fluorescence signal  $f_n(x, y)$  and the noise sources, as described in chapter 3. There are mainly two types of noise [?, ?] sequentially embedded into the image. One is the shot noise generated in the photon collection process, and it follows a Poisson distribution. The other is the excess noise generated during the electron multiplying process, and it follows a Gaussian distribution. The probability distribution of the image noise is the convolution of the two distributions. Similar to Eq.(4.6), we obtain

$$I_n(x, y) \doteq f_n(x, y) + N(0, \sigma_n^2(x, y)) \quad (1.7)$$

$N$  is a Gaussian noise with zero-mean and variance  $\sigma_n^2(x, y) = 2(G_n(x, y) + b_n(x, y))$ . To make this relation valid, each pixel value is divided by the product of EM gain and video chain gain [?, ?] which can be measured or found in the user manual of the microscope.

### 1.2.2 The Feature Estimation Framework

The goal is to find the set of particle features  $\{x^{(k)}, y^{(k)}, z^{(k)}, r^{(k)}, c^{(k)}\}_{k=1}^K$  that maximizes the posterior probability (MAP) given the image dataset  $\{I_n\}_{n=1}^N$  and the axial profiles  $\{h_n\}_{n=1}^N$  of the

evanescent field, i.e., maximizing the energy:

$$E = \log p \left( \{x^{(k)}, y^{(k)}, z^{(k)}, r^{(k)}, c^{(k)}\}_{k=1}^K \mid \{I_n, h_n\}_{n=1}^N \right) \quad (1.8)$$

It is difficult to obtain the analytical expression of the above energy. Instead, we try to maximize the alternative energy:

$$E = \log p \left( \{G_n, b_n\}_{n=1}^N, \{c^{(k)}\}_{k=1}^K \mid \{I_n, h_n\}_{n=1}^N \right) \quad (1.9)$$

The energy  $E$  is a function of the particle features and the background. We partition each 2D image plane into two regions:  $\Omega_n = \{(x, y) \mid G_n(x, y) \geq \delta\}$  and its complement  $\Omega_n^c = \{(x, y) \mid G_n(x, y) < \delta\}$ . Here,  $\delta$  is a very small constant (0.002 in experiments). We define  $I_{\Omega_n} = \{I_n(x, y) \mid (x, y) \in \Omega_n\}$  and  $I_{\Omega_n^c} = \{I_n(x, y) \mid (x, y) \in \Omega_n^c\}$ . Also, we define  $G_{\Omega_n}$ ,  $G_{\Omega_n^c}$ ,  $b_{\Omega_n}$ , and  $b_{\Omega_n^c}$  in a similar way. Since  $G_{\Omega_n^c} \approx \{0\}$ , it can be ignored. Assuming the noises on individual pixels are statistically independent, and using Bayes' rule and ignoring constant terms, the above energy can be decomposed as:

$$E = E_1 + E_2 + E_3 + E_4 + E_5 \quad (1.10)$$

$$E_1 = \sum_{n=1}^N \log p(I_{\Omega_n^c} \mid b_{\Omega_n^c}) \quad (1.11)$$

$$E_2 = \sum_{n=1}^N \log p(I_{\Omega_n} \mid G_{\Omega_n}, b_{\Omega_n}) \quad (1.12)$$

$$E_3 = \sum_{n=1}^N \log p(b_{\Omega_n} \mid b_{\Omega_n^c}) \quad (1.13)$$

$$E_4 = \log p \left( \{c^{(k)}\}_{k=1}^K, \{h_n\}_{n=1}^N \mid \{G_{\Omega_n}\}_{n=1}^N \right) \quad (1.14)$$

$$E_5 = \log p(\{G_{\Omega_n}\}_{n=1}^N) \quad (1.15)$$

We take three steps to solve the optimization problem.

In the first step, we find the initial values of the features and use them to estimate each region  $\Omega_n$ , which will be described in section 5.2.3.

In the second step, we find  $b_{\Omega_n^c}$  which maximizes the energy  $E_1$ . In the region  $\Omega_n^c$ ,  $I_n(x, y) \approx b_n(x, y) + N(0, \sigma_n^2(x, y))$ . Since the background is smooth,  $b_{\Omega_n^c}$  is just the smoothed version of  $I_{\Omega_n^c}$ , which can be obtained by using the local smoothing algorithm in [?].

In the third step, we find  $\{G_{\Omega_n}, b_{\Omega_n}\}_{n=1}^N$  and  $\{c^{(k)}\}_{k=1}^K$  which maximize the summation of the

other energy terms. To find the optimal solution, we use iterated conditional modes (ICM) with deterministic annealing. The energy terms  $E_2$  and  $E_3$  have been defined in chapter 4. Here we simply re-write those equations in the multi-angle situation.

The term  $E_2$  is calculated by using Eq.(5.7), which is given by

$$E_2 = - \sum_{n=1}^N \sum_{(x,y) \in \Omega_n} \frac{(G_n(x,y) + b_n(x,y) - I_n(x,y))^2}{\sigma_n^2(x,y)} \quad (1.16)$$

Here, we ignore the terms that only contain the variance  $\sigma_n^2(x,y)$ . Eq.(5.16) is essentially a nonlinear fitting.

We define the background  $b_n(x,y)$  in the region  $\Omega_n$  as

$$b_n(x,y) = \sum_{k=1}^K \omega_n^{(k)}(x,y) b_n^{(k)} \quad (1.17)$$

Here,  $b_n^{(k)}$  is a scalar variable,  $\omega_n^{(k)}(x,y) \propto G_n^{(k)}(x,y)$ , and  $\sum_{k=1}^K \omega_n^{(k)}(x,y) = 1$ . Roughly speaking,  $b_n^{(k)}$  is the background intensity near the Gaussian component  $G_n^{(k)}(x,y)$ .

The term  $E_3$  is defined by

$$E_3 = - \sum_{n=1}^N \sum_{(x,y) \in \Omega_n} \frac{(b_n(x,y) - \tilde{b}_n(x,y))^2}{\tilde{\sigma}_n^2(x,y)} \quad (1.18)$$

Here,  $\tilde{b}_n(x,y)$  in the region  $\Omega_n$  is obtained by linear interpolation from the background  $b_n(x,y)$  in the region  $\Omega_n^c$ . The variance is calculated as  $\tilde{\sigma}_n^2(x,y) = 2\tilde{b}_n(x,y)$ .

The term  $E_4$  measures how well the axial profiles fit the features, which is give by

$$E_4 = - \sum_{k=1}^K \sum_{n=1}^N \frac{\left(a_n^{(k)} - c^{(k)} h_n(z^{(k)})\right)^2}{\sigma_n^2(x^{(k)}, y^{(k)})} \quad (1.19)$$

Assuming the features of the particles are uniformly distributed, the term  $E_5$  is just a range constraint on the features.

### 1.2.3 Initialization

First, at each xy-location, the average value of the images taken at all the angles is calculated, i.e.,  $\bar{I}_n(x,y) = \frac{1}{N} \sum_{n=1}^N I_n(x,y)$ . Then we apply the initial detection method described in chapter

4, to the resulting 2D image. After the initial xy-positions, radii, and fluorescence amplitudes are obtained, the initial values of the other features are estimated by using Eq.(5.19). Hence, the initial values of the features are obtained.

### 1.3 Method Evaluation

The proposed method is evaluated on synthetic image datasets generated in different scenarios. The simulation method is presented in chapter 3. Figure 5.1 shows some examples of simulated images.

We are interested in finding out the optimal depth configuration, because in real experiments, we can only use two angles due to the relatively low angle-switching speed of the laser beam. A depth configuration refers to a set of two penetration depths,  $\{d_n\}_{n=1}^2$ . The first depth  $d_1$  is fixed to be 100nm in the simulation. The second depth  $d_2$  is allowed to vary in a large range. We add a special depth  $d_2 = \infty$  achieved when the incident angle is less than the critical angle, and the axial profile of the light field can still be modeled as a special decay function  $h_2(z) = I_{02}e^{-z/d_2}$  with  $d_2 = \infty$ .

Each dataset corresponds to a fixed depth configuration, a fixed z-position, a fixed background noise level, and a fixed cell thickness. In a dataset, the z-positions of the particles are the same, and their xy-positions are uniformly distributed in the xy-plane, and their real radii are uniformly distributed from 25 to 50nm. The SNR of a particle in a set of images  $\{I_n\}_{n=1}^2$  is defined by  $SNR = \frac{1}{2} \sum_{n=1}^2 \left( a_n^{(k)} / \sigma_n^{(k)} \right)$ , and  $k$  is the index of the particle. The noise variance is calculated as  $(\sigma_n^{(k)})^2 = 2 \left( a_n^{(k)} + b_n(x^{(k)}, y^{(k)}) \right)$  according to Eq.(5.7), and  $a_n^{(k)}$  is calculated using Eq.(5.6). The fluorophores in the background are uniformly distributed. The background noise level is defined to be the ratio  $\lambda = c_b/c^{(k)}$ . Here,  $c_b = 2\pi\sigma_P^2\rho_b$ , and  $\rho_b$  is the background fluorescence density defined in Eq.(3.14).

The feature estimation method is evaluated on each dataset, using two performance metrics. The first one is the root mean square error (RMSE) of the estimated z-positions, defined by

$$RMSE = \sqrt{\frac{1}{M} \sum_{m=1}^M ((\hat{z}^{(m)} - z^{(m)})^2 + (\hat{z}^{(m)} - z^{(m)})^2)} \quad (1.20)$$

Here,  $z^{(m)}$  is the “true” z-position of a particle indexed by  $m$ , and  $\hat{z}^{(m)}$  is the estimated z-position of the particle.

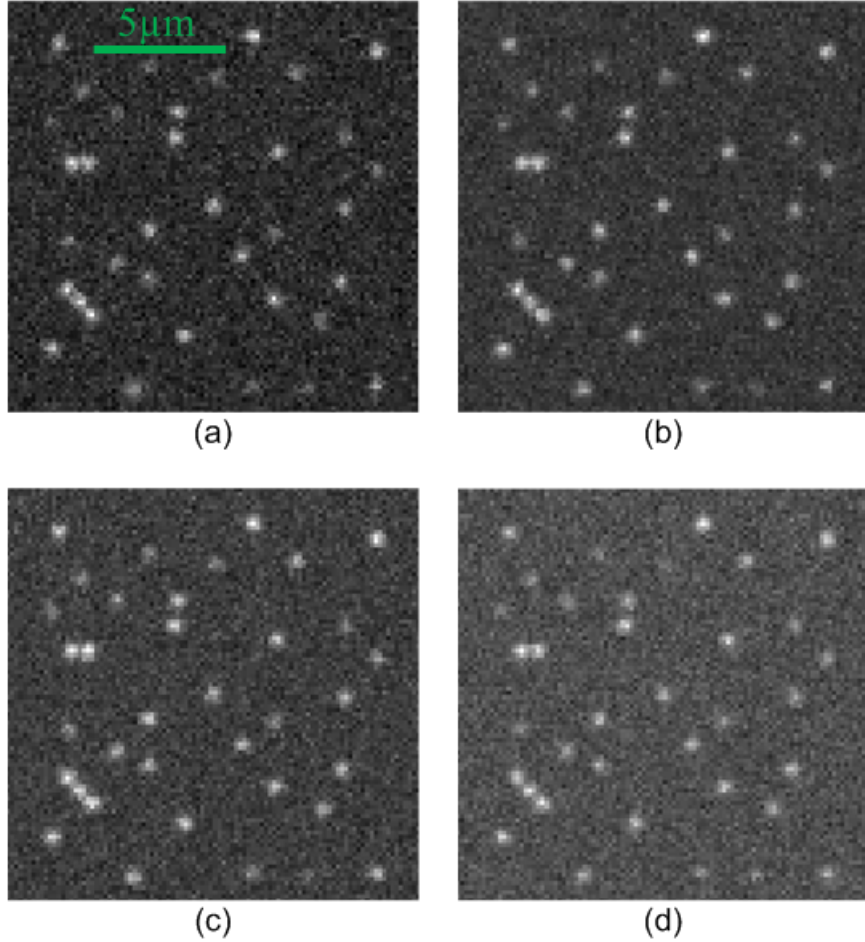


Figure 1.1: Examples of synthetic images (1pixel=160nm). (a)  $d=100\text{nm}$ , (b)  $d=200\text{nm}$ , (c)  $d=400\text{nm}$ , (d)  $d=\infty$ .

The second one is the mean absolute percentage error (MAPE) of the estimated total intensities, defined by

$$MAPE = \frac{1}{M} \sum_{m=1}^M |\hat{c}^{(m)} - c^{(m)}| / c^{(m)} \quad (1.21)$$

Here,  $c^{(m)}$  is the “true” total intensity of a particle indexed by  $m$ , which is calculated using Eq.(5.5).  $\hat{c}^{(m)}$  is the estimated total intensity of the particle.

The two metrics are calculated for the estimation result on each dataset. In Eq.(5.20) and Eq.(5.21),  $M$  represents the total number of correctly detected particles from the same dataset, and it is between 1000 and 1600.

Since xy-positions can be estimated with very good accuracy just by using single-angle TIRFM

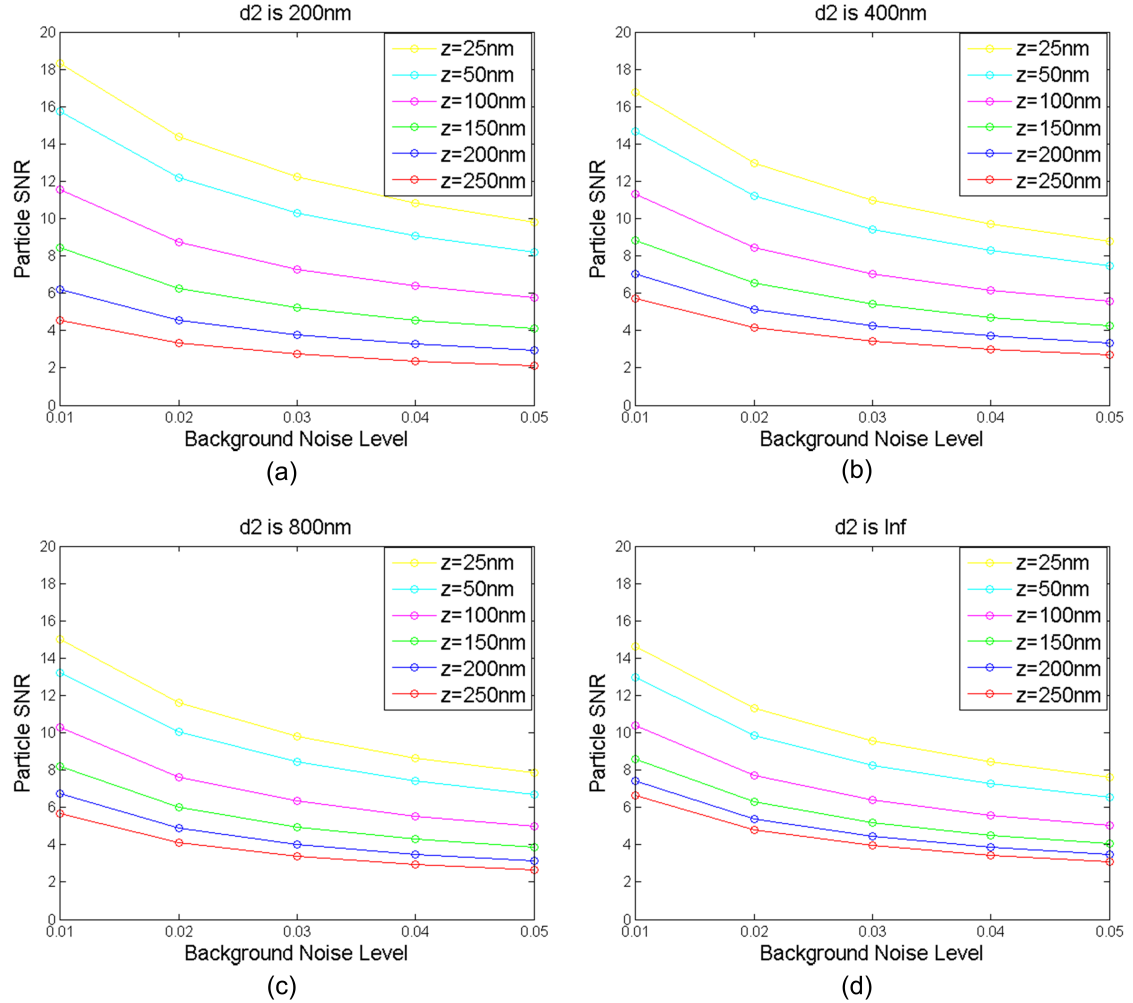


Figure 1.2: Particle SNR in different scenarios

as shown in chapter 4, then xy-position estimation results are omitted.

### Evaluation With Different Depth Configurations

We test four depth configurations:  $\{d_1 = 100\text{nm}, d_2 = 200\text{nm}\}$ ,  $\{d_1 = 100\text{nm}, d_2 = 400\text{nm}\}$ ,  $\{d_1 = 100\text{nm}, d_2 = 800\text{nm}\}$ , and  $\{d_1 = 100\text{nm}, d_2 = \infty\}$ . Cell thickness along the z direction is set to be 1 micron. As the second depth  $d_2$  increases, particle SNR decreases, as shown in Figure 5.2. The performance curves are shown in Figure 5.3 and 5.4. When the second depth gets larger, all the estimation accuracies increase. The best performance is achieved with the configuration  $\{d_1 = 100\text{nm}, d_2 = \infty\}$ .

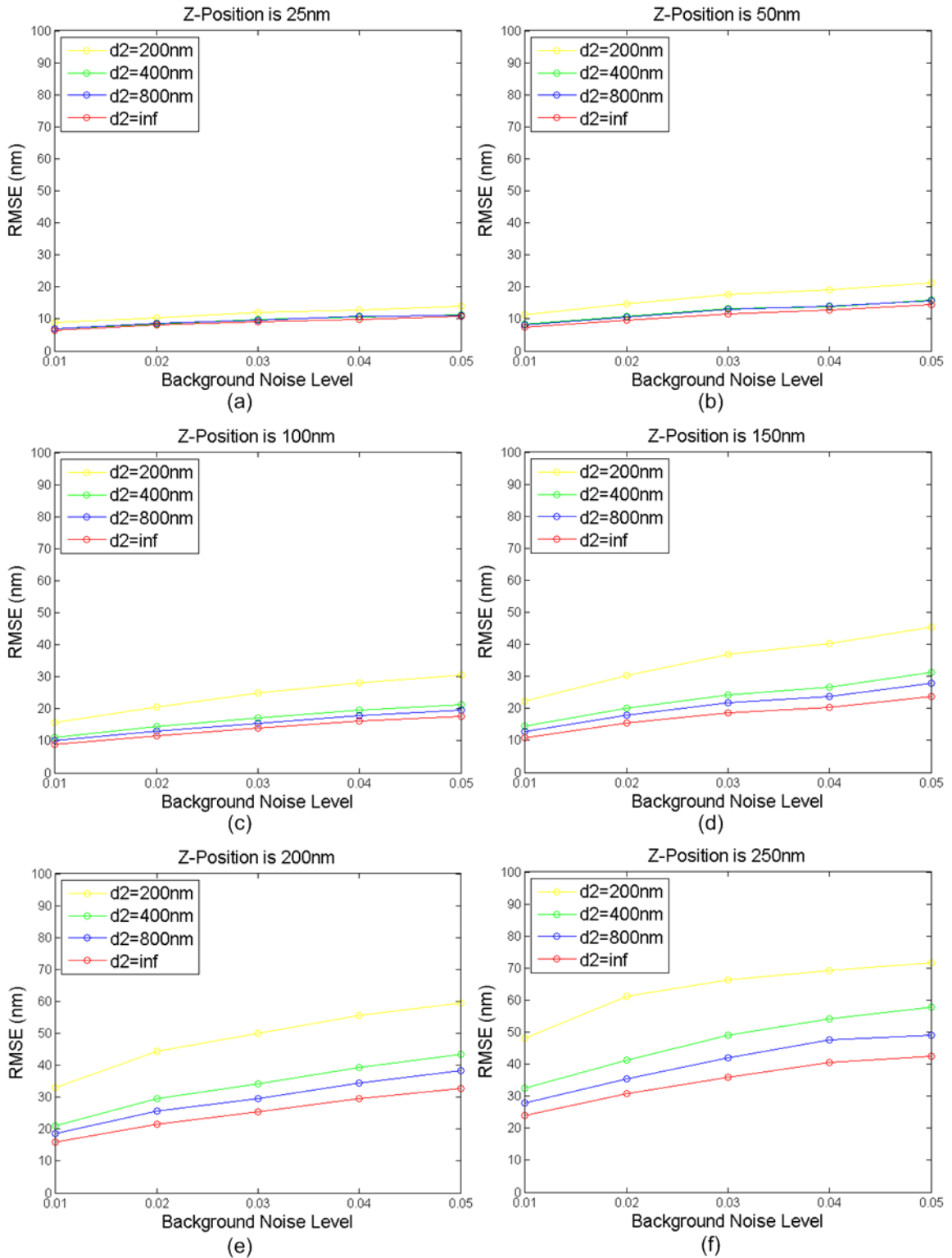


Figure 1.3: Accuracy of the estimated z-positions in different scenarios

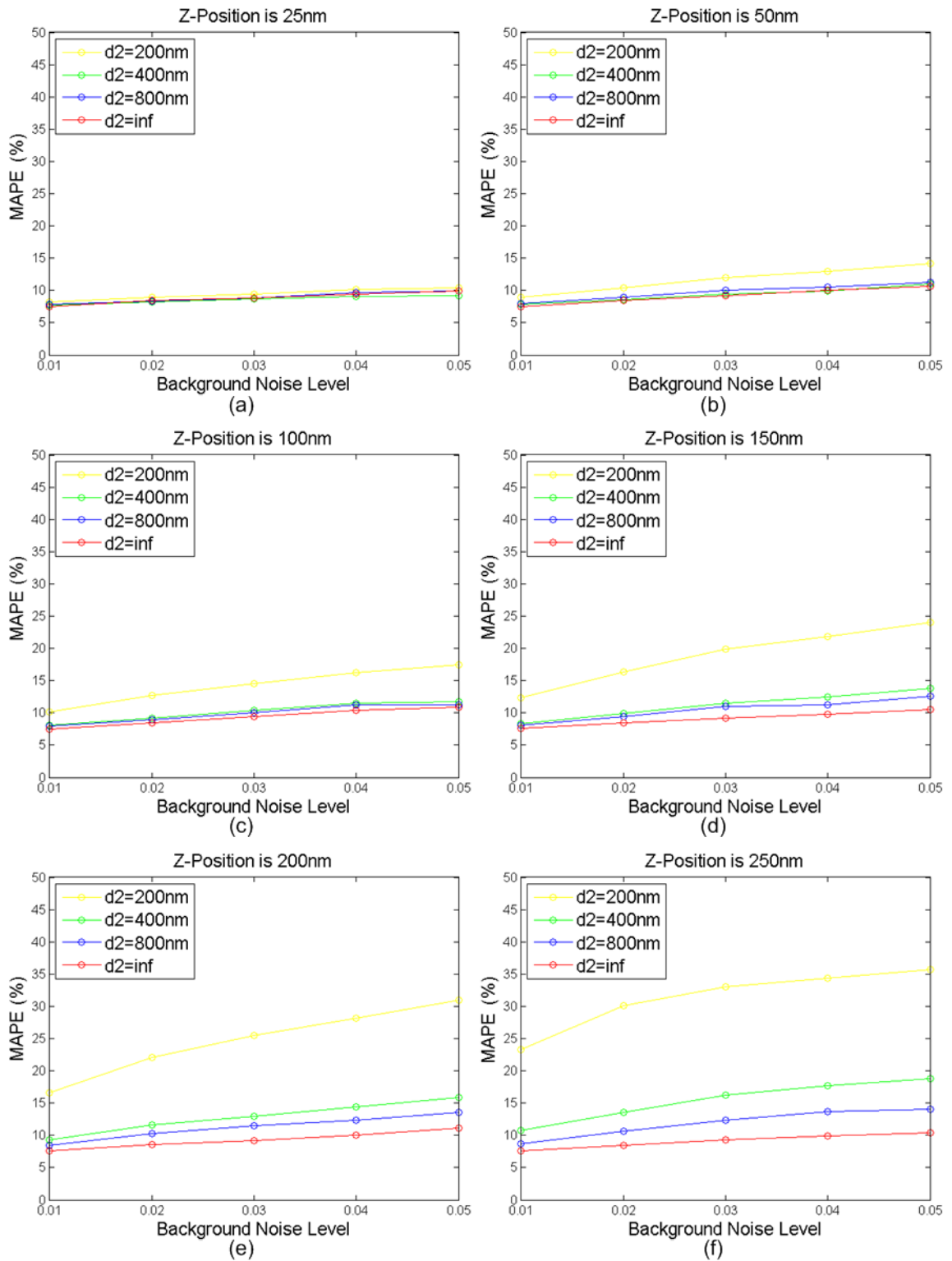


Figure 1.4: Accuracy of the estimated total intensities in different scenarios

The above results show that the accuracy of z-position estimation increases as the second depth increases, as shown in Figure 5.5. This relationship can be explained by using a simple example. Let's assume we have two data points  $I_1 = cI_{01}e^{-z/d_1}$  and  $I_2 = cI_{02}e^{-z/d_2}$  from the same particle, then we obtain

$$\begin{bmatrix} 1 & -\frac{1}{d_1} \\ 1 & -\frac{1}{d_2} \end{bmatrix} \begin{bmatrix} \log(c) \\ z \end{bmatrix} = \begin{bmatrix} \log(I_1/I_{01}) \\ \log(I_2/I_{02}) \end{bmatrix} \quad (1.22)$$

In real applications, both the z-position  $z$  and the total intensity  $c$  are unknown. If the two depths  $d_1$  and  $d_2$  get closer to each other, then the first matrix on the left side of Eq.(5.22) will be more ill-conditioned, and then the accuracy will be lower. Therefore, we need the second depth  $d_2$  to be larger to make better estimation.

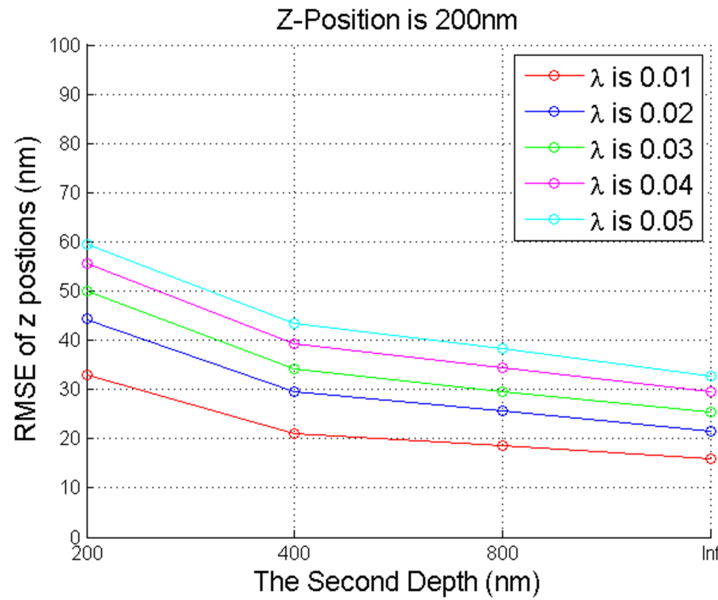


Figure 1.5: Accuracy of the estimated z-position when varying the second depth  $d_2$  and the background noise level  $\lambda$ . The “true” z-position is 200nm.

## Evaluation With Different Cell Thickness

In the above simulations, cell thickness along the z direction is fixed to be 1 micron. The thickness of the fibroblast cells used in experiments is usually between 1 and 3 microns [?, ?]. The thickness is the lowest around cell edges, and the highest around cell nuclei. We test the method with the depth configuration  $\{d_1 = 100\text{nm}, d_2 = \infty\}$  using different cell thicknesses. As the cell thickness increases, particle SNR decreases, as shown in Figure 5.6. The estimation results are shown in Figure 5.7 and 5.8. The estimation accuracy of the total intensities almost does not depend on the z-positions. All the accuracies decrease as the cell thickness becomes larger. Therefore, to get reliable results from real data, we should exclude the image regions near cell nuclei.

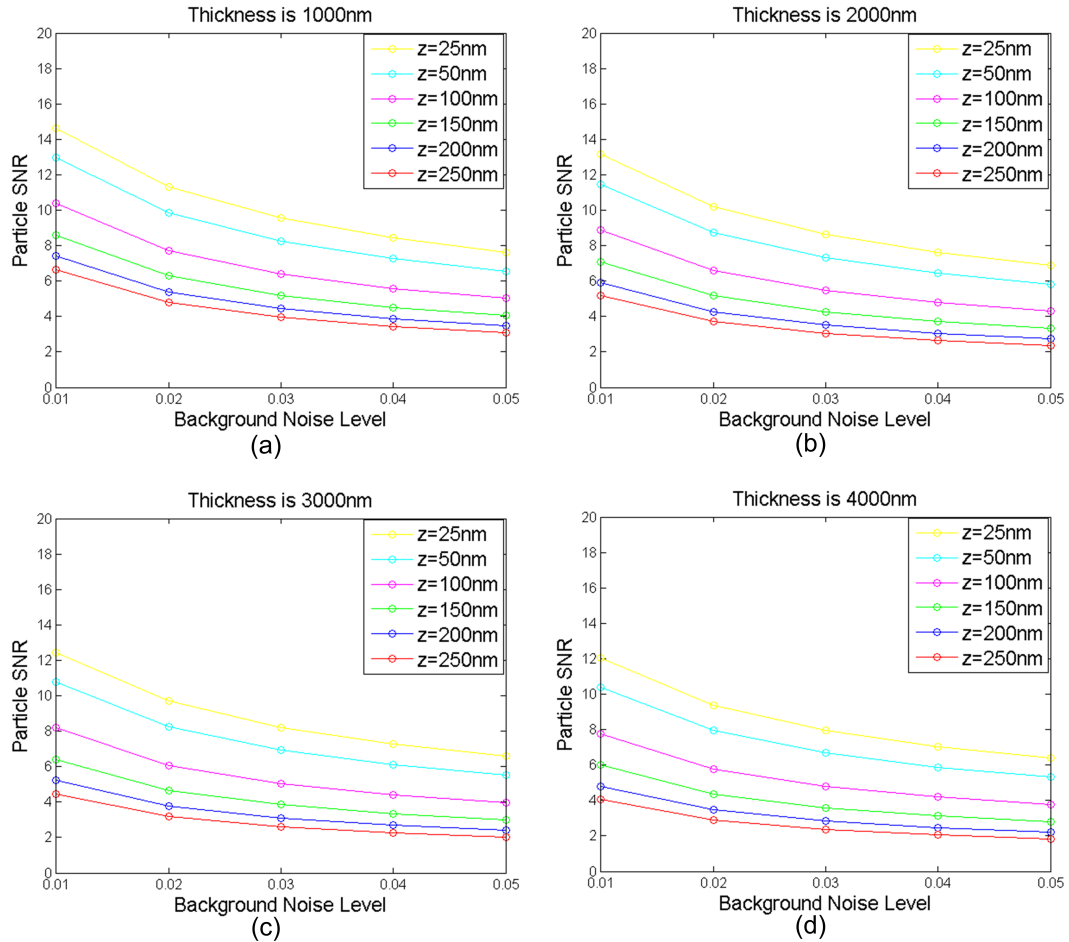


Figure 1.6: Particle SNR in different scenarios

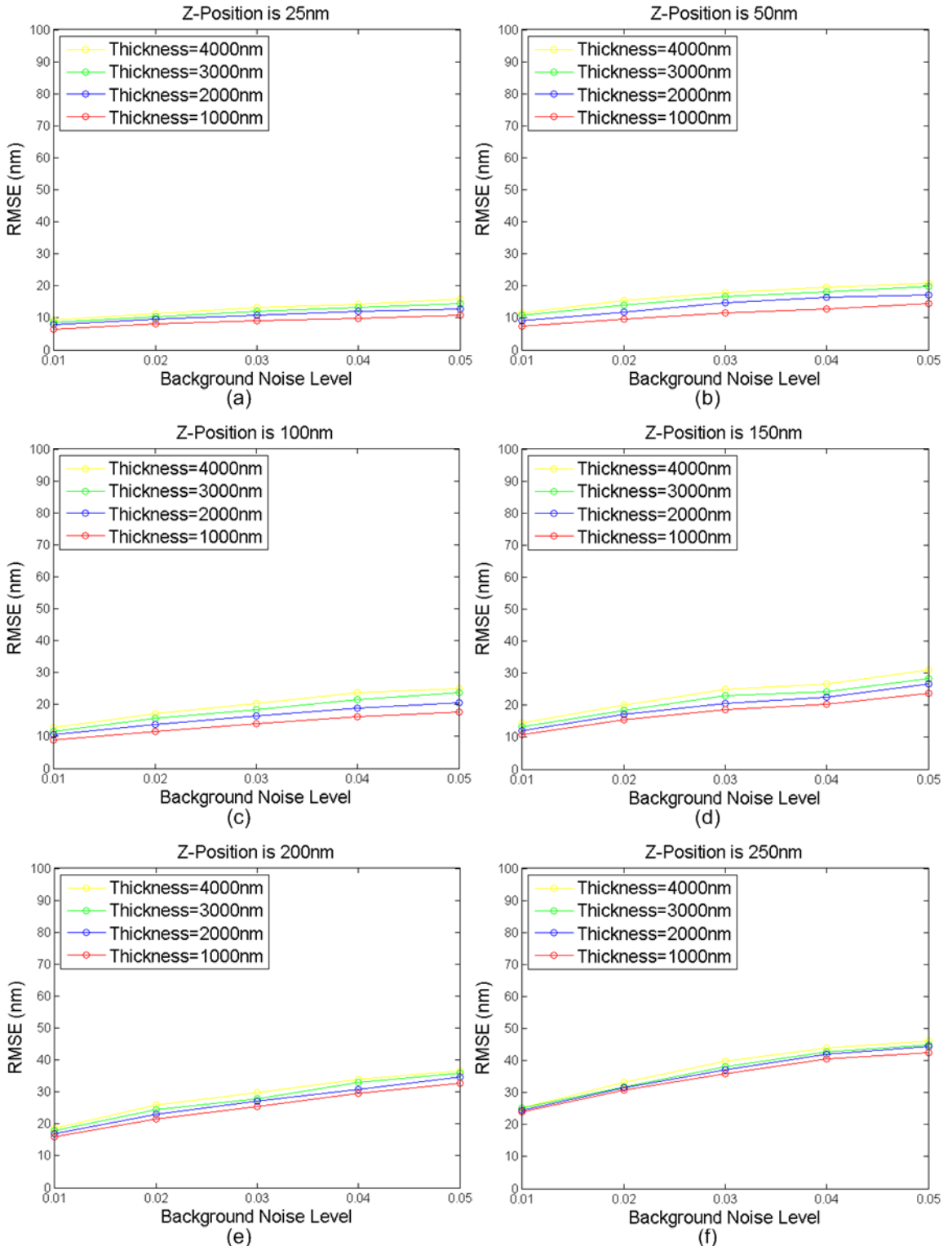


Figure 1.7: Accuracy of the estimated z-positions in different scenarios

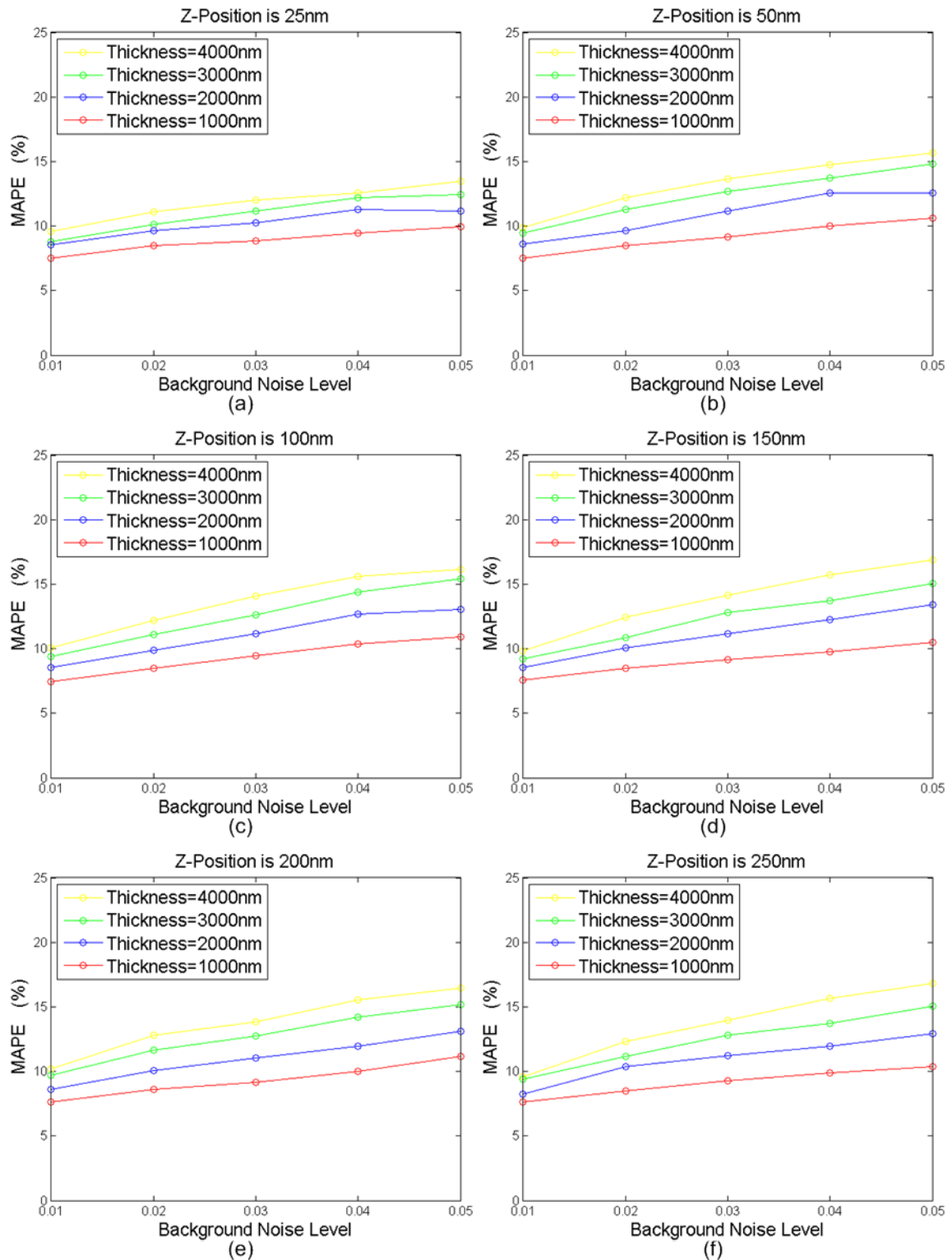


Figure 1.8: Accuracy of the estimated total intensities in different scenarios

## Evaluation With the Parameters From the Real Experiment

According to the experiment described in the next section 5.4, we use the depth configuration  $\{d_1 = 64\text{nm}, d_2 = \infty\}$ , and set the cell thickness along the z direction to be 2 microns, and set the background noise level to be 0.02. The result is shown in Figure 5.9.

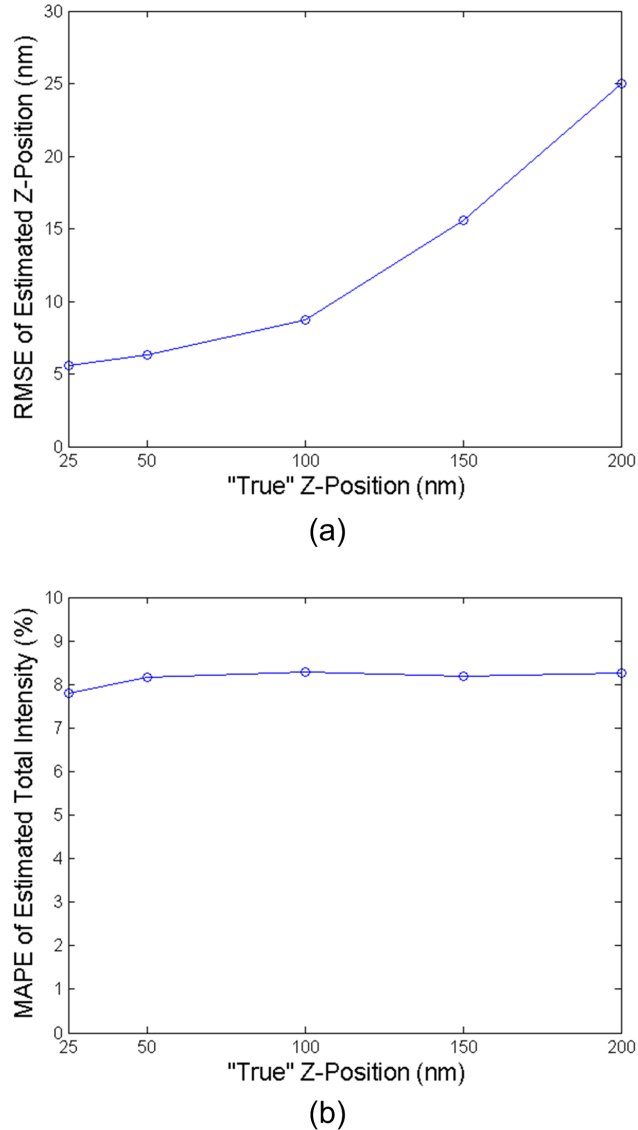


Figure 1.9: (a) RMSE of the estimated z-positions when varying the “true” z-position. (b) MAPE of the estimated total intensities when varying the “true” z-position.

## 1.4 Application to Studying Motion Patterns of CCP Particles

To obtain real data, mouse fibroblast cells were prepared, and clathrin coated pits were fluorescently labeled, and then images were acquired by Nikon Ti-E Eclipse inverted microscope with Apo TIRF 100 $\times$  oil objective lens (NA 1.49) and Andor iXon 897 EMCCD camera. Since the acquisition rate is relatively low (1 frame per angle per half second), we use only two angles. The first one corresponds to the depth  $d = 64nm$ , and the second one corresponds to the special depth  $d = \infty$ . In total, we obtained four datasets. Examples of the images are shown in Figure 5.10.

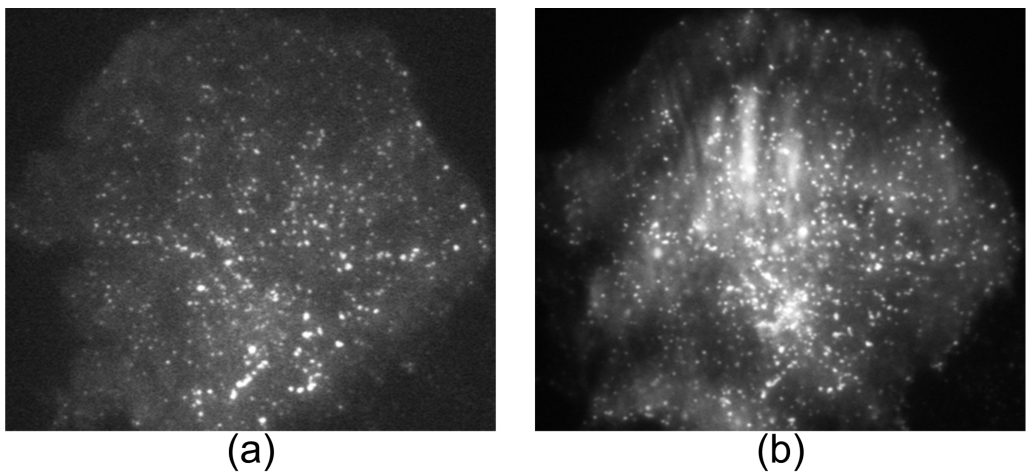


Figure 1.10: Examples of the images. (a) An image of a cell with  $d = 64nm$ . (b) An image of the same cell with  $d = \infty$ .

The intensities in the regions near cell nuclei are very high, and these regions are excluded before the analysis. The background noise level on the selected image regions is less than 0.02. The position estimation result from a selected image region is visualized in Figure 5.11.

We are interested in studying motion patterns of CCP particles, which will help us to design appropriate models for particle tracking. To obtain reliable trajectories, we select the regions where particle density is low, and apply the detection method described in this chapter, and link the detected particles between frames using nearest neighbor criterion. In the CME process as described in section 1 of chapter 1, the movement of each particle is mainly caused and constrained by two factors. First, tiny molecules in cytosol randomly hit each particle during the whole process. Second, the neck of each particle prevents it from going far away from its connection point on the cell membrane. By analyzing two types of distributions related to the two factors, we are able to

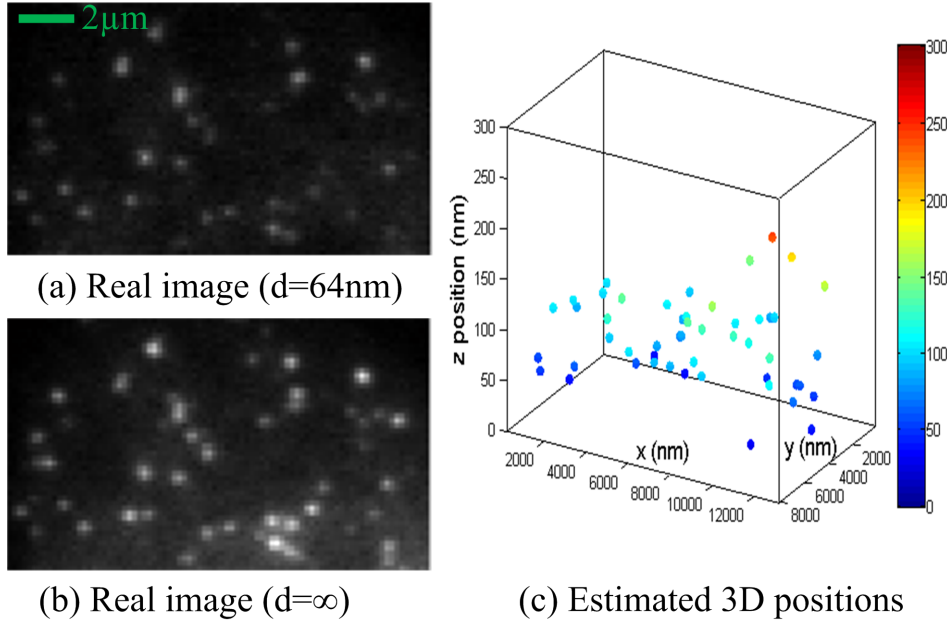


Figure 1.11: Estimation result on a real image region.

design the motion models.

Firstly, we calculate the empirical probability density functions (Epdfs, i.e., normalized histograms) of the displacements (i.e.,  $x_t - x_{t-1}$ ,  $y_t - y_{t-1}$ , and  $z_t - z_{t-1}$ ), as shown in Figure 5.12.  $(x_t, y_t, z_t)$  represents the 3D position of a particle at time  $t$  (frame index). The displacements (e.g.,  $x_t - x_{t-1}$ ) are calculated from the recovered trajectories. The result suggests that it could be Brownian motion.

Secondly, we calculate the empirical probability density functions (Epdfs, i.e., normalized histograms) of the deviations from motion centers (i.e.,  $x - x_c$ ,  $y - y_c$ , and  $z - z_c$ ), as shown in Figure 5.12. Here,  $(x, y, z)$  represents the 3D position of a particle, and the time index  $t$  on each position is omitted.  $(x_c, y_c, z_c)$  represents the motion center of the particle, and it is estimated by taking the average of the positions in the particle's trajectory. The deviations (e.g.,  $x - x_c$ ) are calculated from the recovered trajectories. The result suggests that the motion is center-constrained.

Thus, to describe the motion of a particle, we decide to use two types of motion models: one to describe the random motion, and the other one to describe the motion constraint imposed by the link between the particle and the cell membrane. The two models will be presented in chapter 6.

As mentioned in chapter 4, we want to study the effect of the molecular compound, MbCD, in clathrin mediated exocytosis, and particle lifetimes need to be measured. Since CCP particles just

move around their motion centers, 2D TIRFM is enough for measuring the lifetimes.

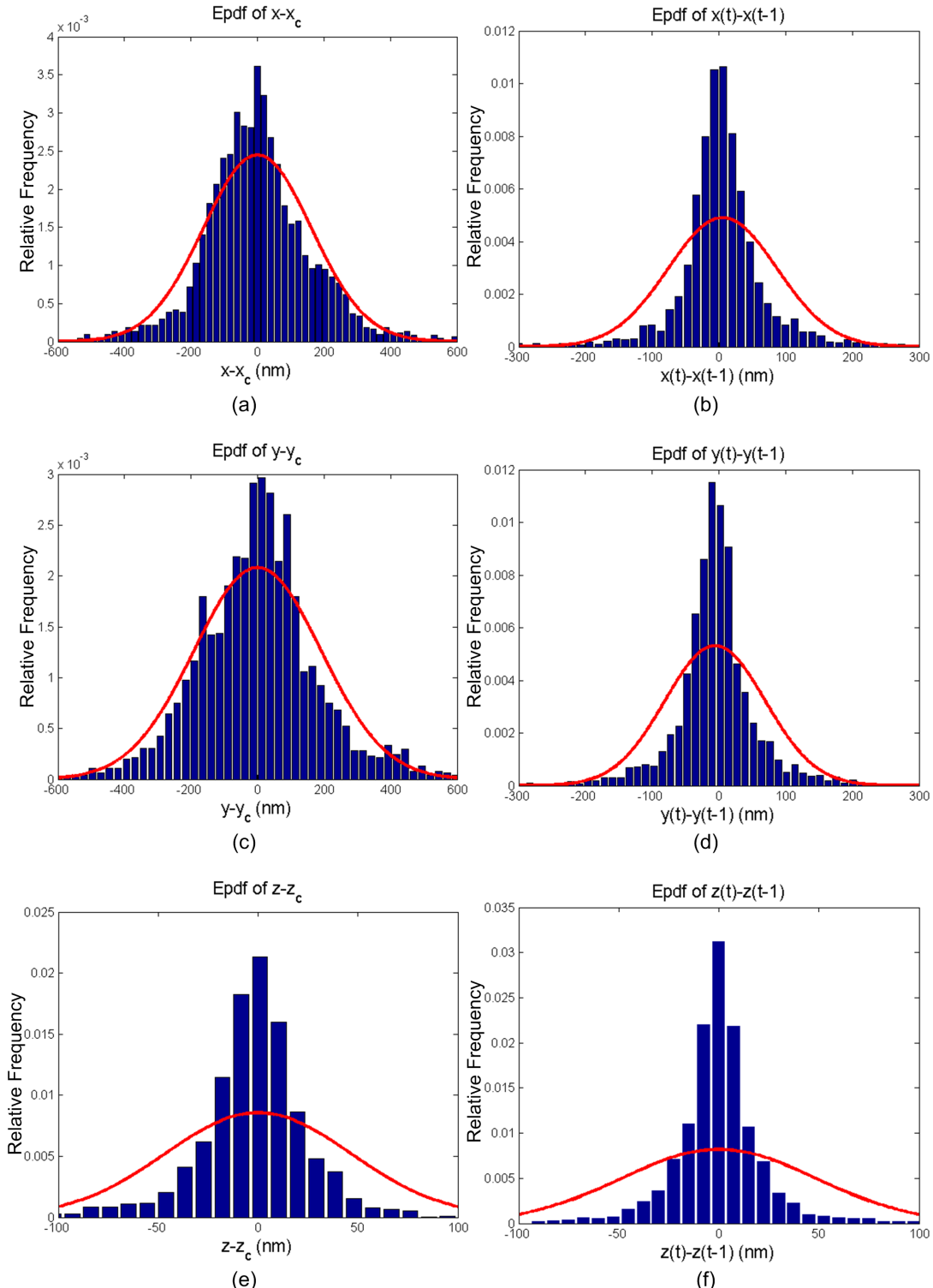


Figure 1.12: Left column: distributions of  $x - x_c$ ,  $y - y_c$ , and  $z - z_c$ . Right column: distributions of  $x_t - x_{t-1}$ ,  $y_t - y_{t-1}$ , and  $z_t - z_{t-1}$ . The red curves show the fitted Gaussian distribution functions.

## 1.5 Conclusion

In this chapter, we have proposed a MAP based method to estimate particle features in 3D using MA-TIRFM. We have evaluated the method under different SNRs and different depth configurations in the simulation. We have applied the method to real data to analyze the motion patterns of CCP particles, which will be used to design the models presented in chapter 6.